Flat bands in twisted double bilayer graphene

Narasimha Raju Chebrolu, Bheema Lingam Chittari, and Jeil Jung*
Department of Physics, University of Seoul, Seoul 02504, Korea

(Received 24 January 2019; revised manuscript received 24 April 2019; published 17 June 2019)

Flat bands with extremely narrow bandwidths on the order of a few millielectron volts can appear in twisted multilayer graphene systems for appropriate system parameters. Here we investigate the electronic structure of a twisted bi-bilayer graphene, or twisted double bilayer graphene, to find the parameter space where isolated flat bands can emerge as a function of twist angle, vertical pressure, and interlayer potential differences. We find that in twisted bi-bilayer graphene the bandwidth is generally flatter than in twisted bilayer graphene by roughly up to a factor of 2 in the same parameter space of twist angle θ and interlayer coupling ω, making it in principle simpler to tailor narrow bandwidth flat bands. Application of vertical pressure can enhance the first magic angle in minimal models at $\theta \sim 1.05^\circ$ to larger values of up to $\theta \sim 1.5^\circ$ when $P \sim 2.5$ GPa, where $\theta \propto \omega/v_F$. Narrow bandwidths are expected in bi-bilayers for a continuous range of small twist angles, i.e., without magic angles, when intrinsic bilayer gaps open by electric fields, or due to remote hopping terms. We find that moderate vertical electric fields can contribute in lifting the degeneracy of the low-energy flat bands by enhancing the primary gap near the Dirac point and the secondary gap with the higher energy bands. Distinct valley Chern bands are expected near 0° or 180° alignments.

DOI: 10.1103/PhysRevB.99.235417

I. INTRODUCTION

Research on twisted hybrid van der Waals two-dimensional 2D materials has recently seen a new surge of interest following experimental observations of exotic quantum phases due to strong electron correlations [1,2] and especially signatures of unconventional superconductivity [3–5] in twisted bilayer graphene (tBG), raising hopes of finding new clues for understanding analogous behaviors seen in more complex systems [6]. In tBG the spatial variation of interlayer coupling modifies the intrinsic Dirac cone band structure of graphene in such a way that the band dispersion is almost completely suppressed at the so-called magic twist angles [7]. When the bandwidth W of these low-energy bands is sufficiently narrow it is possible to achieve the $U/W \gtrsim 1$ condition that makes the effective Coulomb repulsion U more dominant. A considerable body of literature has formed recently on the Coulomb interaction-driven broken symmetry phases [8–14] and superconductivity in tBG flat bands [15–32] in an effort to elucidate the nature of the superconducting phases. Analogous observations of Coulomb interaction-driven correlated phases and superconductivity have been observed in ABC trilayer graphene (TG) on hexagonal boron nitride (hBN) [33–35] where the flattening of the low-energy bands is facilitated by the presence of a vertical electric field that introduces a band gap at the primary Dirac point of a chiral two-dimensional electron gas (2DEG) [36,37], or in twisted gapped Dirac materials [38–40]. It was suggested that the low energy flat bands [41] could have well-defined valley Chern numbers and give rise to spontaneous quantum Hall phases when the band degeneracy is lifted by Coulomb interactions [36,42].

The proposals of flat bands in several types of multilayer graphene materials is suggesting that they can arise in a large variety of 2D material combinations provided that we choose the appropriate intrinsic electronic structure of each layer and their interlayer coupling [42]. In this work we study the flat band bandwidth phase diagram of a twisted BG/BG system, that we refer to as twisted bi-bilayer graphene (tBBG) or twisted double bilayer graphene, which consists of two bilayer graphene units with a twist. We assess for this system the effect of the interlayer coupling strength and the interlayer potential differences between the layers in the resulting bandwidth of the low-energy flat bands. It is expected that the smaller parabolic band dispersion slopes at low energy in a BG can favor the formation of flat bands upon interlayer hybridization. This paper is structured as follows. In Sec. II we introduce the theoretical details of the continuum model Hamiltonian used to formulate the problem. In Sec. III we present the phase diagram of U/W, the flat band bandwidth and gaps as a function of different system parameters, such as the twist angle, the interlayer coupling strength, and the interlayer potential differences due to a vertical electric field. In Sec. IV we discuss the valley Chern number phase diagrams, and then close the paper in Sec. V with the summary and conclusions.

II. MODEL HAMILTONIAN FOR TWISTED BI-BILAYER GRAPHENE

Models proposed in the literature to capture the electronic structure of tBG relied either on tight-binding calculations [43–45] often based on the distance-dependent two center approximation models for the hopping terms between interlayer carbon atoms, or by using other more sophisticated parametrizations [46,47]. The successful formulation of a

*jeiljung@uos.ac.kr

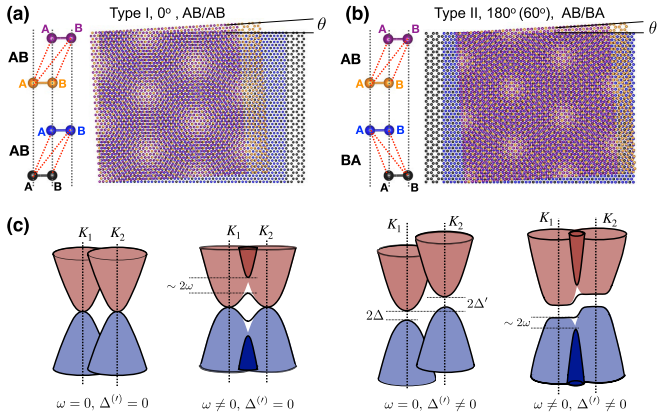

FIG. 1. Moiré pattern created by a twisted bi-bilayer graphene (tBBG) and the commensurate unit cell of two Bernal stacked bilayer graphene aligned (a) near 0° twist angle for type-I AB/AB twisted bi-bilayers, and (b) near 180° (or 60°) twist angles for type-II AB/BA twisted bi-bilayers. Panel (c) represents schematically two uncoupled parabolic bands, the perturbative interband hybridization through the interlayer tunneling ω, the intrinsic bilayer gap (2Δ), and band offset ($2\Delta'$) due to a perpendicular electric field.

rigorous moiré bands theory on the basis of the moiré pattern superlattice [7] allows one to obtain accurate continuum models for the Hamiltonian informed from first-principles calculations [47]. In the present work we extend the continuum model of Bistritzer-MacDonald for the tBG [7] to the case of tBBG. The Hamiltonian of tBBG at valley K that we use captures the interlayer coupling between the twisted layers through a first-harmonic stacking-dependent interlayer tunneling function. Schematic representations of commensurate and twisted BG/BG structures are shown in Fig. 1. We write the Hamiltonian of the twisted top (+) and bottom (−) bilayer graphene Hamiltonian subject to Δ_i intralayer potentials as

$$H_{\rm tBBG}(\theta)=\begin{pmatrix} h_t^+ + \bar{\Delta}_1 & t_s^+ & 0 & 0 \\ t_s^{+\dagger} & h_b^+ + \bar{\Delta}_2 & T(\mathbf{r}) & 0 \\ 0 & T^\dagger(\mathbf{r}) & h_t^- + \bar{\Delta}_3 & t_s^- \\ 0 & 0 & t_s^{-\dagger} & h_b^- + \bar{\Delta}_4 \end{pmatrix}, \tag{1}$$

where $h_{t/b}^\pm = h_{t/b}(\pm\theta/2)$ such that the relative twist angle between the bilayers is θ. The top and bottom BG are labeled through the positive/negative (+/−) rotation signs, while in turn we have top/bottom (t/b) graphene layers within each BG that are coupled through the matrices $t_s^\pm$ that we define later. The site potentials for each graphene layer Δ_i are mapped on its sublattices through $\bar{\Delta}_i = \Delta_i \mathbb{1}$ where $i = 1, 2, 3, 4$ are the layer labels from top to bottom, and $\mathbb{1}$ is a 2×2 identity matrix. Potential differences can give rise to band gaps at the primary Dirac point of each BG and shift the associated band edges. We will discuss later on the effects of these intralayer potentials in the electronic structure of the flat bands. The Hamiltonian of graphene is given by $h_l^\pm(\theta) = h^\pm(\theta) + \delta(\mathbb{1} - l s\sigma_z)/2$ where the second term adds a $\delta = 0.015$ eV sublattice potential at the higher energy dimer sites at the t/b layers $l = \pm$ [48], that depends on AB or BA stacking $s = \pm$, respectively. The Dirac Hamiltonian given by $h(\theta) = \upsilon_F \hat{R}_{-\theta}\mathbf{p}\cdot\sigma_{xy}$ includes a phase shift due to a rotation $\hat{R}_{-\theta}$ such that $e^{\pm i\theta_{\mathbf{p}}} \to e^{\pm i(\theta_{\mathbf{p}}-\theta)}$, where $\sigma_{xy} = (\sigma_x, \sigma_y)$ and σ_z are the graphene sublattice pseudospin Pauli matrices, and the momentum is defined in the xy plane $\mathbf{p} = (p_x, p_y)$, where we assume K valley unless stated otherwise. The Fermi velocity $\upsilon_F = \upsilon_0$ defined from $\upsilon_i = \sqrt{3}|t_i|a/2\hbar$ is related to the intralayer nearest-neighbor hopping term $t_0 = -2.6$ eV within the local density approximation (LDA) [49], while an enhanced $t_0 = -3.1$ eV and *ab initio* interlayer tuning better captures the experimental moiré band features [50]. The interlayer coupling model of a bilayer graphene is given by

$$t_{\rm AB}^\pm = \begin{pmatrix} -\upsilon_4\pi^{\pm\dagger} & -\upsilon_3\pi^\pm \\ t_1 & -\upsilon_4\pi^{\pm\dagger} \end{pmatrix}, \qquad t_{\rm BA}^\pm = t_{\rm AB}^{\pm\dagger} \tag{2}$$

satisfying $t_{s=+} = t_{s=-}^\dagger$ for AB or BA ($s = \pm 1$) stacking-dependent interlayer coupling that consists of a minimal coupling term $t_s = t_1(\sigma_x - is\sigma_y)/2$ plus remote hopping contributions through $t_3 = 0.283$, $t_4 = 0.138$ terms, giving rise to trigonal warping and electron-hole asymmetry. The $\pi^\pm$ operators include the phases due to $\pm\theta/2$ layer rotation. The type-II AB/BA bi-bilayers near 180° alignment can be modeled by controlling the stacking of bottom BG from AB to BA by using $s = -1$ for the bottom BG. The interlayer tunneling is defined as the Hamiltonian matrix element at the Dirac point $t_1 = H_{BA'}(K, \vec{d}_{\rm AB})$ between B and A' sites from bottom to top layer for AB stacking when both atomic sites are vertically aligned and assume $t_1 = 0.361$ eV at zero pressure within LDA [48]. We can identify the interlayer tunneling with the first harmonic expansion coefficient of the interlayer coupling such that $t_1 = 3\omega$ [47], and for simplicity we use the same AB stacking tunneling within each Bernal BG and the twisted interfaces. The minimal model approximation uses $\delta = t_3 = t_4 = 0$ in Eq. (1). The presence of remote hopping terms will lead to broadening of the low-energy flat bands and enhancement in electron-hole asymmetry. This behavior is not strange since the t_3 trigonal warping widens the range of band touching points at three points away from the Dirac point at directions connecting the K points with Γ [48], and the t_4 term breaks the intrinsic electron-hole symmetry of bilayer graphene [51].

The moiré Brillouin zone (mBZ) orientation is preserved when the top and bottom graphene layers rotate symmetrically in opposite senses. In the small-angle approximation the interlayer coupling Hamiltonian is given by

$$T(\mathbf{r}) = \sum_{j=0,\pm} e^{-i\mathbf{Q}_j\mathbf{r}} T_{l,l'}^j, \tag{3}$$

where the three $\mathbf{Q}_j$ vectors $\mathbf{Q}_0 = K\theta(0,-1)$ and $\mathbf{Q}_\pm = K\theta(\pm\sqrt{3}/2, 1/2)$ are proportional to twist angle θ and $K = 4\pi/3a$ is the Brillouin zone corner length of graphene, whose lattice constant is $a = 2.46$ Å, and here the indices l, l' label the sublattices of neighboring twisted surface layers. The interlayer coupling matrices between the two rotated adjacent layers are given by

$$T^0 = \begin{pmatrix} \omega' & \omega \\ \omega & \omega' \end{pmatrix}, \qquad T^\pm = \begin{pmatrix} \omega' & \omega e^{\mp i2\pi/3} \\ \omega e^{\pm i2\pi/3} & \omega' \end{pmatrix} \tag{4}$$

using a form that distinguishes interlayer tunneling matrix elements $\omega = \omega_{BA'}$ and $\omega' = \omega_{AA'}$ for different and same sublattice sites between the layers. The convention taken here for the T^j matrices [47] assumes an initial AA stacking

configuration $\tau = (0, 0)$ and differs by a phase factor with respect to the initial AB stacking $\tau = (0, a/\sqrt{3})$ [7]. The greater interlayer separation c compared to the carbon-carbon distances a_{CC} lead to slowly varying interlayer tunneling function $T(\mathbf{r})$ and the moiré patterns can often be accurately described within a first-harmonic approximation [7,47]. In this limit, and assuming no corrugation effects, the interlayer coupling strength can be well approximated by a single parameter $\omega = \omega'$ whose value was calculated within LDA to be $\omega \sim 0.113$ eV when averaged for every stacking at a fixed interlayer distance $c_{AB} = 3.35$ Å of AB stacking. A somewhat weaker $\omega \sim 0.098$ eV is expected when the interlayer relaxations for farther AA interlayer distance $c_{AA} = 3.57$ Å within LDA is accounted for in the averaging process [47]. The interlayer tunneling matrix elements $H_{ll'}(K, \vec{d})$ are evaluated at the Dirac point K for a commensurate system with stacking sliding vector $\vec{d}$ through the lattice Fourier transform of the distant real-space hopping terms connecting the sites l and l'. The tunneling matrix elements ω, ω' for twisted systems are obtained averaging over all possible commensurate stacking configurations given by the integral

$$\omega_{ll'} = \int_{\text{cell}} d\vec{d}\, H_{ll'}(K, \vec{d}) \simeq \sum_s \frac{H_{ll'}(K, \vec{d}_s)}{3} \tag{5}$$

that in the first-harmonic approximation can be approximated by taking the average of the sum over the three symmetric stacking configurations $s = \text{AA}, \text{AB}, \text{BA}$ at their respective equilibrium interlayer distances [47]. Because tunneling between interlayer sublattices in graphene on graphene vanish at symmetric stackings s when they are not vertically aligned we have

$$\omega = \omega_{AB'} = \omega_{BA'} \simeq \frac{H_{BA'}(K, d_{\text{AB}})}{3}, \tag{6}$$

$$\omega' = \omega_{AA'} = \omega_{BB'} \simeq \frac{H_{AA'}(K, d_{\text{AA}})}{3}. \tag{7}$$

Using Eqs. (6) and (7) at zero pressure and using the EXX+RPA equilibrium distances for each stacking [52] we get $\omega = 0.12$ eV for c_{AB} such that $t_1 = 3\omega = 0.36$ eV, close to the LDA interlayer coupling in Bernal BG, and $\omega' = 0.098$ eV for c_{AA}, which is incidentally rather close to the interlayer tunneling from explicit integrations in $\vec{d}$ in Ref. [47]. The effects of atomic relaxation in the moiré patterns can have non-negligible effects in the details of the electronic structure for both intralayer potentials and interlayer coupling that can be captured with higher-order harmonics in the moiré G vectors [53]. It was also noted that in tBG unequal interlayer coupling values $\omega \neq \omega'$ enhances the gap between the low-energy flat band and its neighboring higher-energy band [12]. The band structures for type-I AB/AB structures near 0° alignment calculated for the minimal tBBG model are shown in Fig. 2 both for rigid unrelaxed $\omega = \omega'$ and out-of-plane

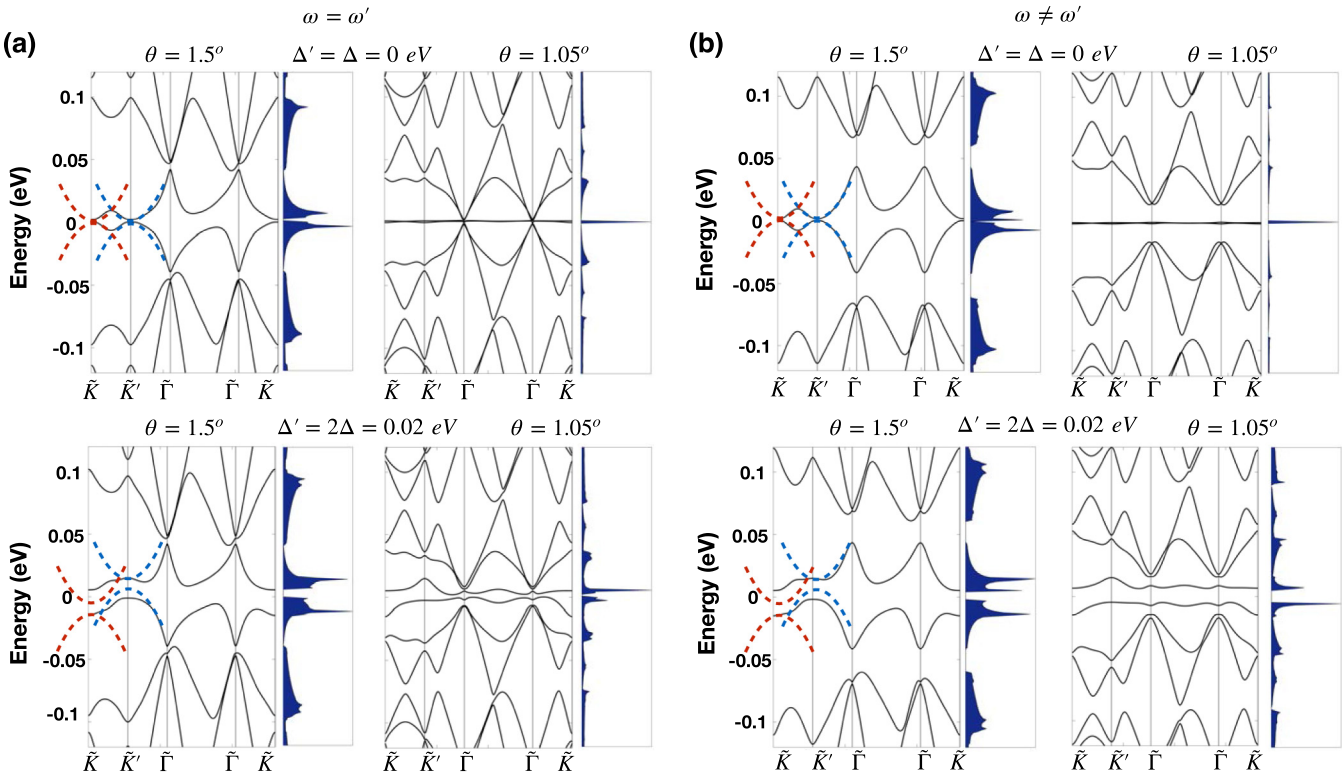

FIG. 2. Band structures of bi-bilayer graphene for $\theta = 1.5°, 1.05°$, for zero and finite interlayer potential difference parameters Δ, Δ'. The parabolic dotted lines are a guide to the eye for the original position of the bilayer graphene band edge in the absence of interlayer tunneling between the BG. The addition of an interlayer potential difference through the Δ' parameters introduces a separation between the low-energy flat bands roughly proportional to the interlayer potential difference between the top and bottom outer layers of tBBG. For a system with Fermi velocity $v_F = 1.0 \times 10^6$ m/s we show the (a) band structures calculated with a single parameter interlayer coupling $\omega = \omega' = 0.12$ eV, and (b) band structures calculated with $\omega' = 0.1$ and $\omega = 0.12$ eV with different intersublattice tunneling values that enhances the gap between the flat bands and the neighboring higher energy bands.

relaxed interlayer tunneling values $\omega \neq \omega'$. In the case of tBG it was noted that the magic angle follows the $\theta \propto \omega/\upsilon_F$ proportionality [54] where the magic angles grow with increasing interlayer coupling strength. Hence, an enhanced $\upsilon_F = 1.0 \times 10^6$ m/s (or $t_0 = -3.1$ eV), together with *ab initio* tunneling $\omega = 0.12$ eV, $\omega' = 0.098$ eV from Eqs. (6) and (7) leads to similar low-energy bands as the LDA $\upsilon_F = 0.84 \times 10^6$ m/s (or $t_0 = -2.6$ eV) combined with weaker $\omega = 0.1$ eV and $\omega' = 0.08$ eV values. In the calculations to follow we use the enhanced Fermi velocity of $\upsilon_F = 1.0 \times 10^6$ m/s together with the *ab initio* interlayer tunneling ω and ω' based on Eqs. (6) and (7) compatible with EXX+RPA equilibrium distances. Our calculations have used a configuration space with variable cutoff in momentum space of a radius of up to $6G_1 = 24\pi\theta/(\sqrt{3}a)$ using Hamiltonian matrices with sizes as large as 676×676 such that $\theta \gtrsim \omega/(12\pi|t_0|)$ to obtain converged results in the limit of small θ and large ω.

An important distinctive feature of tBBG with respect to tBG is that we have an additional control knob to change the electronic structure through a perpendicular external electric field that modifies the interlayer potential Δ_i values in Eq. (1). The potential drops introduced by an external electric field could be modeled through the parameter set $\Delta_1 = -\Delta_4$, $\Delta_2 = -\Delta_3$, redefined as $\Delta_1 = (\Delta + \Delta')/2$, $\Delta_2 = (-\Delta + \Delta')/2$ in terms of 2Δ, the interlayer potential difference within each BG, and $2\Delta'$ the potential difference between the BG. We will use the relation $\Delta' = 2\Delta$ to introduce equal interlayer potential drops of Δ' between the consecutive layers to model the effects of an electric field. A qualitatively different interlayer potential configuration consists in having the electric fields point in opposite directions at each BG. This could be done by grounding the tBBG device and using equipotential top/bottom gates to accumulate charges of the same sign at the outer layers. The potential distribution of this case can be modeled by $\Delta_1 = -\Delta_2 = -\Delta_3 = \Delta_4 = \Delta$, where the reversal of the relative mass sign between the top and bottom BG can modify the topology of the resulting flat bands. Distinct band topologies are thus expected for a system subject to a perpendicular electric field near 180° (or 60°) alignment where for the same mass sign the chirality of the bands at K are reversed.

III. FLATBANDS AS A FUNCTION OF TWIST ANGLE, ELECTRIC FIELDS, AND PRESSURE

In the following we discuss the electronic structure results and the moiré flat band bandwidth in tBBG as a function of system parameters such as twist angle θ, the interlayer coupling ω tunable by pressure, and interlayer potential differences due to an electric field, in search of the optimal conditions for finding isolated low-energy flat bands near the Fermi level. The interlayer potential differences due to an electric field are modeled combining potential differences between the layers within each BG (Δ) and inter-BG potential offset (Δ'), which are related to each other through $\Delta' = 2\Delta$ that can lift the degeneracy of the flat bands.

In the band structures resulting from the minimal model shown in Fig. 2 for a twist angle of $\theta = 1.5°$, we can still distinguish features of the original BG band structure at the Dirac cones, and can identify the band structure near the magic angle $\theta = 1.05°$ of tBG. The first important observation is that the overall bandwidths of the low-energy bands in tBBG are almost half of those corresponding to tBG for a similar range of θ and ω parameter values, suggesting that the tBBG system is generally more suitable for the generation of narrow bandwidth flat bands than in tBG. This is shown in Fig. 3 where we represent the bandwidth as a function of twist angle θ for fixed values of interlayer coupling ω and as a function of ω for fixed θ values. From the bandwidth versus θ dependence we can observe that the bandwidths remain below 10 meV for every twist angle below and around the first magic angle. Likewise, the bounce off of the bandwidth for increasing ω past the critical value at the first magic angle have maxima that are roughly half of those seen in tBG [54]. We thus expect that in tBBG the twist angle control does not need to be as precise as in tBG to maintain a moderately narrow bandwidth on the order of ~10 meV for twist angles smaller than ~1°. Inclusion of remote hopping terms results in band gaps near charge neutrality for sufficiently large twist angles and widening of the bandwidths with respect to the minimal model, as shown in Fig. 4. The trigonal warping term in BG generates several band touching points in the vicinity of the Dirac point, and introduces particle-hole symmetry breaking of sufficient relevance especially when we apply an external electric field. In Fig. 4 we compare the band structures of the minimal model and the more complete model that includes the remote hopping parameters, both for type I near 0° and type II near 180° alignments. For the complete Hamiltonian we include the remote hopping terms

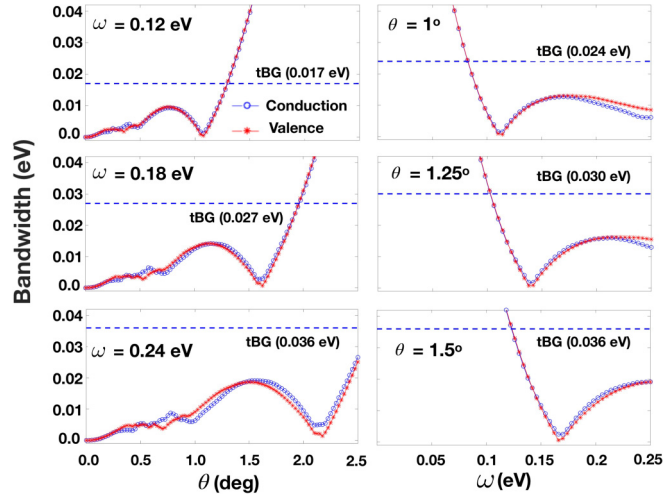

FIG. 3. Variation of flat band bandwidth for $\Delta = \Delta' = 0$ eV as a function of interlayer coupling strength and twist angle for the rigid continuum model with $t_0 = -2.6$ eV. The bandwidths in tBBG are narrower by roughly a factor of 2 when compared with the bandwidths in tBG with similar system parameters, where the dotted horizontal lines represent the bandwidth of tBG at the belly maxima. Left panel: Flatband bandwidth as a function of twist angle θ at different interlayer couplings $\omega = 0.12, 0.18, 0.24$ eV. We observe that the bandwidth changes nonmonotonically with the twist angle and goes through a series bandwidth minima. Right panel: Flat band bandwidth as a function of ω, at different twist angles $\theta° = 1°, 1.25°, 1.5°$. We can observe a steep initial reduction in the bandwidth followed by a mild bump for increasing ω.

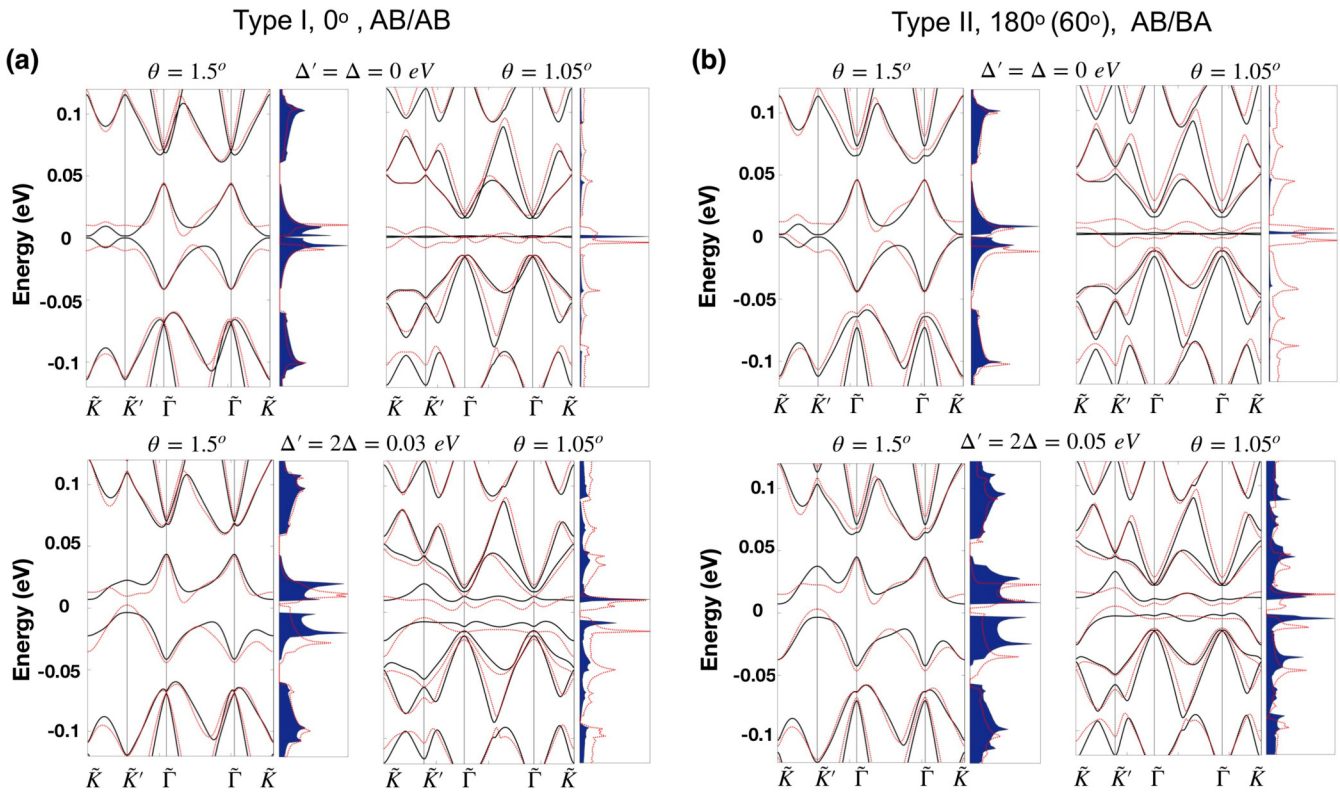

FIG. 4. Comparison of the minimal and remote hopping Hamiltonian model that includes the trigonal warping t_3, intrinsic electron-hole asymmetric t_4 terms, and higher-energy dimer site potential δ. The band structures of the minimal model are in black, and those that include the remote hopping terms are in dotted red lines. The remote hopping terms generally widen the minimal model flat bands, and can introduce primary band gaps δ_p near charge neutrality for large twist angles. Appropriate electric fields can compress the bandwidth, while maintaining band isolation through the primary δ_p and secondary gaps δ_s. We distinguish the (a) band structures for type I near 0° alignment and (b) for type II near 180° alignment that show distinct electronic structures and responses to electric fields.

t_3 and t_4, the site potential offset δ between the high energy dimer sites, and interlayer coupling ω and ω' in Eqs. (6) and (7) evaluated at the equilibrium out-of-plane relaxed lattice distances.

The second important observation is the tunability of the primary and secondary band gaps accompanied by a variation in bandwidth due to an electric field, as illustrated in Fig. 4. Even for a twist angle ∼1.5° considerably greater than the minimal model magic angle of ∼1° the low-energy bands can remain isolated thanks to the primary δ_p and secondary δ_s gaps. These gap values are obtained from the difference between the maximum (minimum) energy of the flat band and the minimum (maximum) energy of the neighboring higher (lower) band resulting in positive values when there is a gap and giving negative values when there is band overlap. Application of external fields contributes in changing the bandwidth and a relatively narrow bandwidth on the order of ∼25 meV or smaller is achievable for moderate electric fields that introduce interlayer potential differences typically of a few tens of meV. The bandwidths were obtained from the difference between the maximum and minimum band energy for a given band within the mBZ. Band gaps within each BG layer (Δ) and band offsets between BG layers (Δ') are simultaneously present when a perpendicular electric field is applied in the system. It is found that generally Δ' contributes in widening the bandwidth of the low-energy bands.

An important factor for the onset of the interaction-driven ordering is the isolation of the low-energy bands that can be quantified from the primary gap δ_p near charge neutrality and the secondary gap δ_s near the Γ point of mBZ, since greater band isolation reduces screening and strengthens the Coulomb interactions. Hence, the parameter space most likely to observe Coulomb-driven ordered phases should have simultaneously smaller bandwidths W and larger isolation gaps δ_p and δ_s. We can estimate the ratio of $U_{\rm eff}/W$ from the effective three-dimensional screened Coulomb potential

$$U_{\rm eff} = \frac{e^2}{4\pi\varepsilon_r\varepsilon_0 l_M}\exp(-l_M/\lambda_{\rm D}), \tag{8}$$

where the moiré length is $l_M = a/\theta$, and the Debye length $\lambda_{\rm D} = 2\varepsilon_0/e^2 D(\delta_p, \delta_s)$ uses the 2D density of states $D(\delta_p, \delta_s) = 4[|\delta_p|u(-\delta_p) + |\delta_s|u(-\delta_s)]/(W^2 A_M)$ that assumes a value proportional to the band overlap ratio $\delta_{p/s}/W$ when $\delta_{p/s} < 0$, where $u(x)$ is the heaviside step function, $\varepsilon_r = 4$, and we counted four valley-spin degenerate electrons per moiré unit cell area $A_M = \sqrt{3}\,l_M^2/2$ for each filled moiré band. This ratio in Eq. (8) is used to find the parameter space region of twist angle and interlayer electric field with narrow bands and strong effective Coulomb interactions (see Fig. 5). While the parameter region near $\theta \sim 0.5°$ shows the largest $U_{\rm eff}/W$ ratios compared to $\theta \gtrsim 1°$ due to the greater flatness of the bands at small twist angles, the closer proximity of

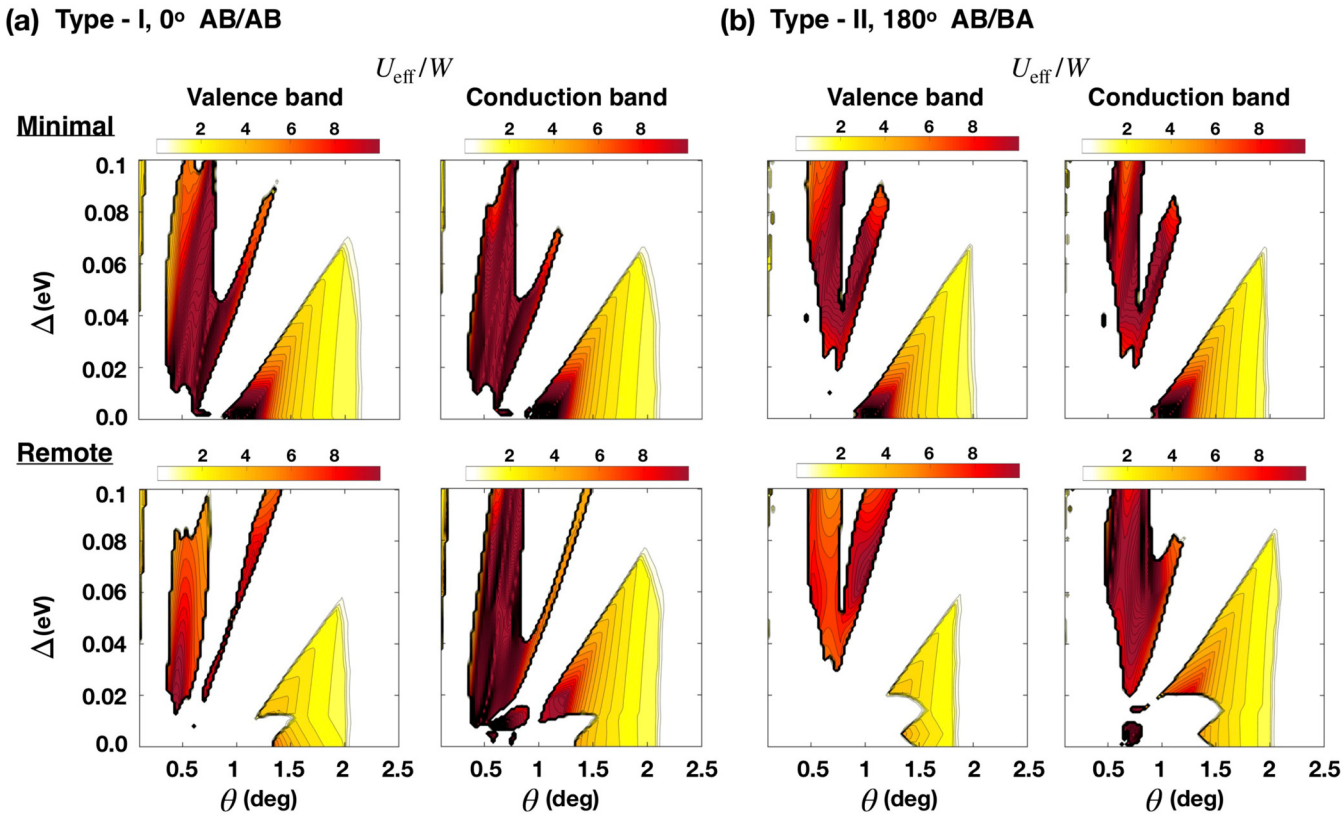

FIG. 5. Colormap phase diagram of U_{eff}/W for the effective Coulomb interaction versus bandwidth W in the parameter space of θ and Δ that indicates the plausible regions where Coulomb interactions can trigger ordered phases. Inclusion of remote hopping terms in the band Hamiltonian of bilayer graphene introduces particle-hole symmetry breaking generally favoring U_{eff}/W for the conduction bands over the valence bands. Islands in the phase diagram are found due to the suppression of U_{eff} in Eq. (8) when neighboring bands overlap, leading to large regions of twist angles between 0.5°–0.8° and 1°–1.6° favorable for interaction-driven broken symmetry phases for Δ values accessible in experiments.

the neighboring energy bands in this regime may enhance the Coulomb screening in a way that is not captured in the screening model we have used. We expect that the electron-hole asymmetry resulting from the intrinsic asymmetry of BG with remote hopping terms can be further affected by the coupling with the substrate, for example by aligning BG with a hexagonal boron nitride substrate which in a heterojunction with single-layer graphene, introduced a strong intrinsic particle-hole asymmetry in the electronic structure [55].

A phase diagram of the bandwidth, the primary gap, and secondary gap as a function of twist angle and external field strength is presented in Fig. 6. For simplicity we have assumed that the potential differences between contiguous layers are given by $\Delta' = 2\Delta$ and are the same for a given electric field, although the precise interlayer potential differences will depend on the screening between the layers. This phase diagram of U_{eff}/W ratios, bandwidths, primary, and secondary gaps both for electrons and holes illustrates the parameter space where the likelihood for finding ordered phases is higher. As a general trend we find a non-negligible asymmetry between electrons and holes, and the possibility of finding states with primary and secondary gaps both at small and large twist angles of $\sim$0.5° and $\sim$1.5° for sufficiently strong electric fields. Due to the almost linear increase of the low-energy bandwidth with increasing twist angle there is a tradeoff between band isolation easier at larger twist angles and bandwidth increase to find the optimum parameter space where the Coulomb interaction effects will be strongest.

Application of pressure is also a useful control knob to tune the electronic structure of 2D materials [4,54,56,57]. In the bandwidth and gaps phase diagram as a function of twist angle and pressure shown in Fig. 7 both for $\Delta^{(\prime)} = 0$ and for $\Delta^{(\prime)} \neq 0$ we can observe that the enhancement of ω through pressure generally compresses the bandwidth of the flat bands. In the minimal model of tBBG the application of pressure leads to a magic angle line

$$\theta_n^\circ = C_n \frac{\omega}{|t_0|} \quad \text{(deg)} \tag{9}$$

whose coefficient values of $C_1 = 27.5$, $C_2 = 10.5$, and $C_3 = 5.6$ agree within 10% with the results obtained for tBG [54], in keeping with the expected band scaling behavior proportional to $\alpha = \omega/(\theta \upsilon_F K)$ [7] (see Supplemental Material [58]). This observation suggests that increase of ω, e.g., through external pressure P [56], should allow one to achieve narrow bandwidth features for larger twist angle θ. This behavior holds both for the minimal model and when remote hopping terms are considered, although the remote hopping terms tend to broaden the bandwidth of the minimal

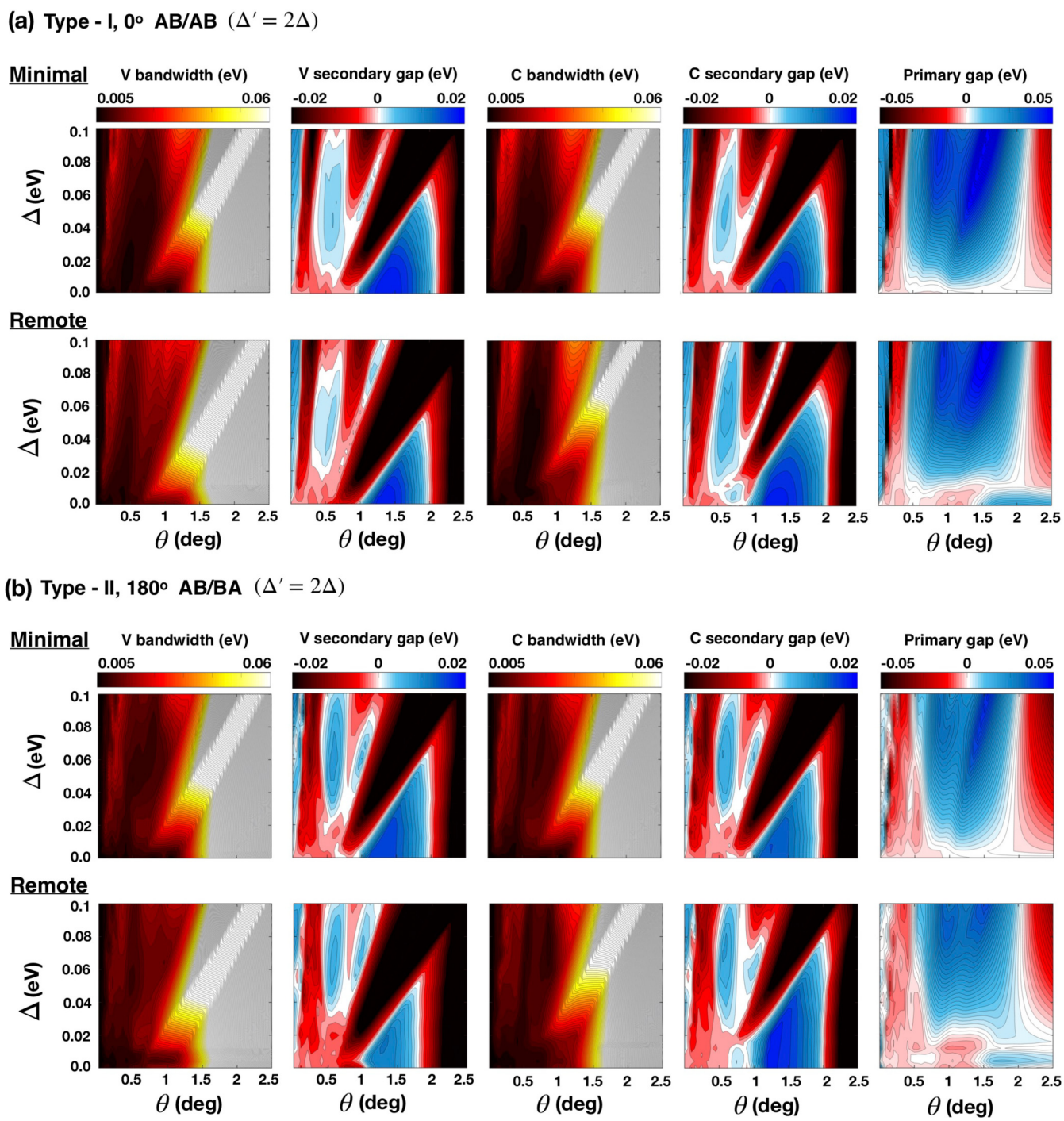

FIG. 6. Variation of flat band bandwidth and band isolation through the primary δ_p and secondary δ_s band gaps for the low-energy valence (V) and conduction (C) bands near charge neutrality as a function of twist angle θ and interlayer potential difference Δ, shown for (a) type I near 0° alignment as a function of θ and Δ, and for (b) type II near 180° alignment, that requires a larger Δ to achieve positive primary gaps δ_p for $\theta \gtrsim 1^\circ$ to simultaneously achieve $\delta_{p/s} > 0$. The remote hopping terms introduce particle-hole symmetry breaking that expands the parameter space where the low-energy flat bands are isolated and generally favors the isolation of the conduction band over the valence bands. Negative values for the gaps indicate overlap with neighboring bands. In the presence of remote hopping terms, simultaneous $\delta_{p/s} > 0$ are expected in the conduction bands for small Δ in the vicinity of $\theta \sim 0.7^\circ$ and in particular around $\theta \gtrsim 1.5^\circ$, for both near 0° and 180° alignments. These regions should be more accessible with scanning probe measurements where vertical electric fields and induced carrier densities are less directly controllable than in top-bottom dual gated devices.

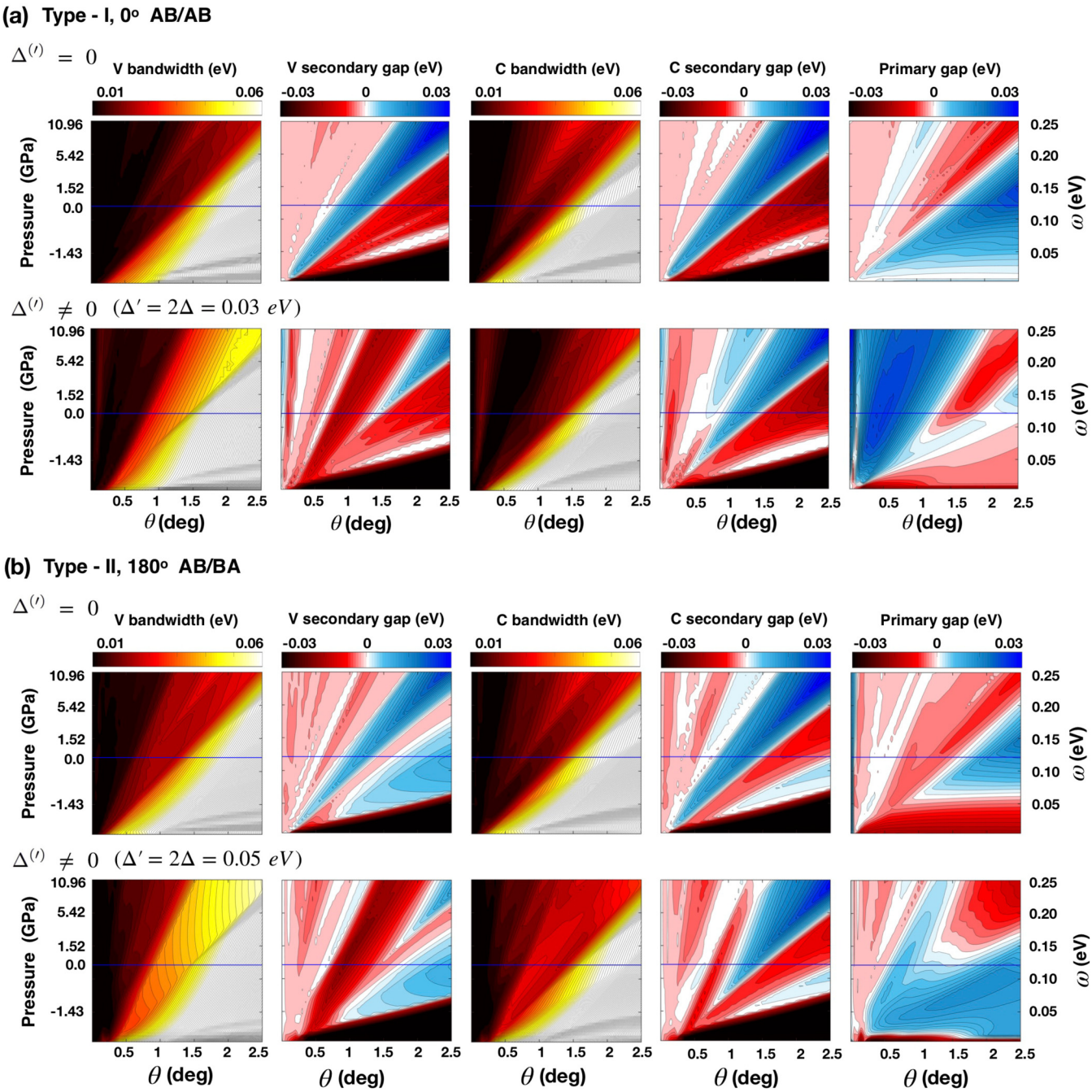

FIG. 7. Phase diagram of bandwidth and band isolation of the flat band through primary δ_p and secondary δ_s gaps with the surrounding bands, calculated both for the valence and conduction flat bands as a function of θ and $\Delta' = 2\Delta$ for (a) type I near 0° alignment, and for (b) type II near 180° alignment. The Hamiltonian model for the above results includes the remote hopping terms and the calculations were carried out for $\Delta' = 0$, and for finite interlayer potential $\Delta' \neq 0$. More phase diagrams for other Δ values and calculations for the minimal model can be found in the Supplemental Material [58].

model (see the Supplemental Material for a comparison of the phase diagrams [58]). The phase diagram also illustrates how pressure can be used to enhance the secondary gaps both for valence and conduction bands, but it can at the same time suppress the primary gap. The phase diagram is modified substantially in the presence of interlayer potential differences $\Delta^{(\prime)} \neq 0$ triggered by a perpendicular electric field, generally widening the bandwidth in the phase diagram and shifting the weights between the primary and secondary gaps. The relationship between P and ω values in the relevant range of pressures between 0 and ~15 GPa is fitted by a second-order polynomial and its positive root:

$$P = A\omega^2 + B\omega + C, \tag{10}$$

$$\omega = A' + \sqrt{B' + C'P}. \tag{11}$$

TABLE I. External pressure $P(\omega_s)$ and associated interlayer coupling $\omega_s(P)$ for commensurate stacking geometries (s = AA,AB,BA) illustrated in Fig. 8. We list the fitting coefficients for $P(\omega)$ in Eq. (10) A (GPa/eV^2), for B (GPa/eV), and C (GPa), and the inverse fit for $\omega(P)$ in Eq. (11) A' (eV), for B' (eV^2), and C' (eV^2/GPa).

	LDA			EXX+RPA		
Stacking (s)	A	B	C	A	B	C
AA	473.6	−22.17	−0.9011	543.3	−61.01	0.735
AB	306.5	−36.56	−0.04339	324.7	−35.47	−0.4671
Stacking (s)	A'	B'	C'	A'	B'	C'
AA	0.0234	0.0025	0.0021	0.0561	0.0018	0.0018
AB	0.0596	0.0037	0.0033	0.0546	0.0044	0.0031

The fitting parameters are listed in Table I and they are found to be valid over a wide range of pressures stretching up to ∼30 GPa and also for negative values down to ∼ − 1 GPa. To obtain the above fitting parameters we have used the relationship between P and interlayer separation c for every stacking of Ref. [52], and the calculations of ω versus c as detailed in Ref. [47]. The explicit fitting functions for these quantities are presented in the Supplemental Material [58]. This approach is different from that in Ref. [54] where the total pressure was obtained from the average of the local pressure values at the same interlayer distance c for every stacking.

IV. TOPOLOGICAL FLAT BANDS IN TWISTED BI-BILAYER GRAPHENE

The presence of moiré superlattices gives rise to avoided gaps between the bands in the mBZ allowing them to have a well-defined valley Chern number in a wide class of twisted multilayer systems [42,59,60], transition-metal dichalcogenides [61], trilayer graphene on hexagonal boron nitride (TG/BN) [36], and for a variety of twisted gapped Dirac materials [39]. For our tBBG system the possibility

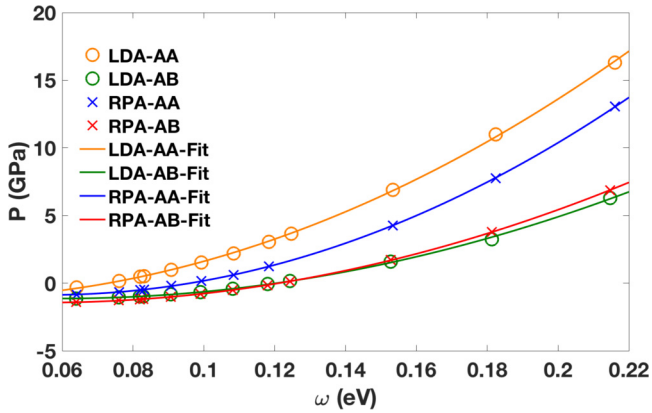

FIG. 8. Interlayer coupling versus pressure for different stacking geometries AA, AB (equivalent to BA) for equilibrium distances calculated within the LDA and EXX+RPA calculations from Ref. [52] that can be fitted through Eqs. (10) and (11) with the parameters in Table I.

of opening a band gap δ_p near charge neutrality through an electric field together with the opening of a secondary gap δ_s with the higher-energy bands makes tBBG an interesting platform to engineer flat bands with well-defined valley Chern numbers that are tunable through an electric field like in TG/BN [36,42]. The valley Chern number phase diagram in Fig. 9 as a function of interlayer potential differences and twist angle indicates the range of Chern numbers $C_\upsilon = 0, \pm1, \pm2, \pm3, \pm4$ expected in these systems. The valley Chern numbers were calculated through

$$C_\upsilon = \int_{\text{mBZ}} d^2\vec{k}\ \Omega_n(\vec{k})/(2\pi) \tag{12}$$

by integrating in the moiré Brillouin zone for each valley the Berry curvature for the nth band through [62]

$$\Omega_n(\vec{k}) = -2\sum_{n'\neq n} \text{Im}\left[\frac{\langle u_n|\frac{\partial H}{\partial k_x}|u_{n'}\rangle\langle u_{n'}|\frac{\partial H}{\partial k_y}|u_n\rangle}{(E_{n'}-E_n)^2}\right], \tag{13}$$

where for every k point we take sums through all the neighboring n' bands, the $|u_n\rangle$ are the moiré superlattice Bloch states, and E_n are the eigenvalues. There are clear qualitative differences between the valley Chern numbers for twist angles near 0° for type-I AB/AB and those near 180° for type-II AB/BA alignments. In the first case the valley Chern numbers between valence and conduction bands are generally opposite in value adding up to a total of zero, while in the second case they are the same number for both valence and conduction bands. These differences are naturally expected if we consider that the chirality of the massive bands at the top and bottom layers that couple to each other are interchanged depending on the alignment. Quantitative modifications in the valley Chern numbers are observed when we compare the phase diagrams of the minimal and remote hopping parameter models as a function of Δ where clear differences in particular for small Δ ∼ 10 meV regions are observed, comparable in magnitude with the band distortions introduced by the remote hopping terms. The vicinity of $\theta \sim 1°$ and low electric field Δ have spots where the valley Chern numbers for the valence and conduction bands differ in magnitude. For sufficiently large values of Δ the valley Chern numbers of the lowest-energy flat bands agree for the minimal and remote hopping parameter models in a large parameter space of twist angles as illustrated in Fig. 10 by showing the band structure and the Berry curvatures used in the valley Chern number calculations. Hence, the topological properties of the bands remain overall relatively robust to small perturbations to the band structures introduced by the remote hopping parameters. The values of the low-energy flat band Chern numbers and those of the neighboring higher-energy bands are gathered in Table II. When the valley Chern numbers between the minimal and remote hopping term models differ they are comparable in a large parameter space.

V. SUMMARY AND CONCLUSIONS

We have extended the Bistritzer-MacDonald continuum model of tBG to investigate the electronic structure of tBBG as a function of twist angle θ, electric fields, and the

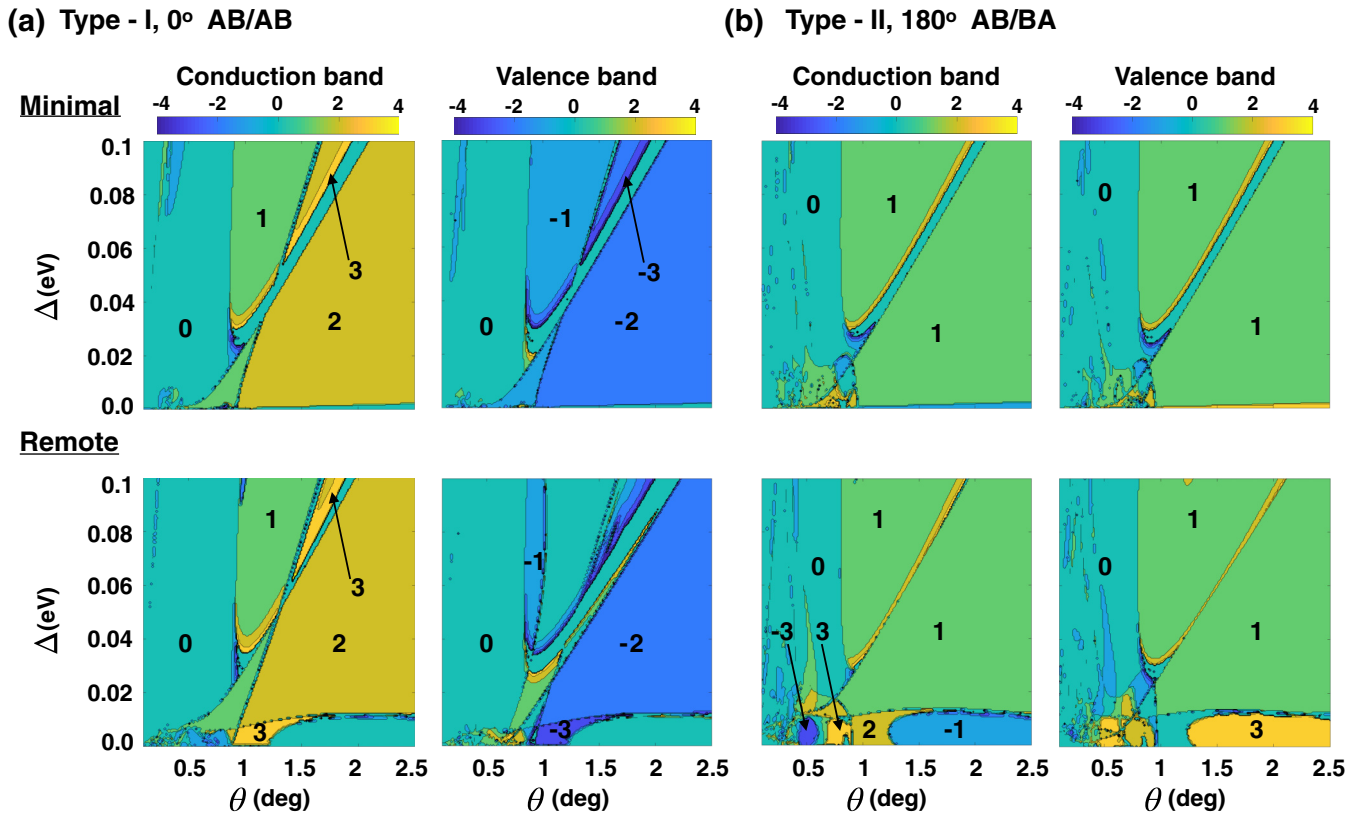

FIG. 9. The K valley Chern number phase diagram of low-energy conduction and valence bands for the minimal model of tBBG (top row) and including the remote hopping parameters (bottom row). Agreement between both models is seen for a large parameter space, although when remote hopping terms are considered we can expect to trigger quantum phase transitions with different valley Chern numbers at moderate values of $\Delta \sim 10$ meV to access regions in phase space where we can expect quantized Hall conductivities at zero magnetic fields, particularly for twist angles $\theta \gtrsim 1^\circ$.

pressure-dependent interlayer coupling. We have considered both the minimal model and also the effects of the remote hopping terms in the band structure calculation of bilayer graphene. The calculated bandwidth phase diagram for the low-energy bands shows that the bandwiths are roughly a factor 2 narrower than those in tBG indicating that tBBG should be more forgiving in the twist angle precision required to access the strongly interacting regime, and for this reason we expect that the narrow band features in tBBG will be observed more simply than in tBG. The possibility of applying a perpendicular electric field is an interesting control knob that allows one to enhance the separation between the flat bands and also influences the gaps with the higher-energy bands favoring a more effective band isolation. At the same time, we find that interlayer potential differences can widen the bandwidths near the first magic angle of the minimal model and smoothen the bandwidth variation to give a continuous range of angles where the bandwidths are narrow. Within the minimal model, the bandwidth phase diagram for zero interlayer potential difference and small perturbations thereof is found to be closely similar to the case of tBG, maintaining the same linear dependence between θ and the interlayer coupling ω for the magic angles, and the inverse proportionality to the Fermi velocity of the graphene layers. Our calculations show that bi-bilayer graphene under a perpendicular electric field can host robust ordered phases for twist angles in the vicinity of $\sim 0.6^\circ$ and near $\sim 1.5^\circ$, with the parameter space for the conduction bands being generally favored over those of the

TABLE II. The Chern numbers table of tBBG for twist angles near the 0° (Type I) and 180° (Type II) alignment with and without remote hopping parameters at the angles $\theta = 1.5^\circ$, 1.05°, and 0.7° whose band structures are represented in Fig. 10. The Chern numbers presented here are for low-energy conduction (C) and valence bands (V), and one higher energy band in each conduction (C + 1) and valence (V − 1) band. The interlayer potentials are, respectively, $\Delta' = 0.03$ eV for $\theta \sim 0^\circ$ and $\Delta' = 0.05$ eV for $\theta \sim 180^\circ$, which are large enough to isolate the low-energy bands.

	Minimal				Remote			
Bands	V (−1)	V	C	C (+1)	V (−1)	V	C	C (+1)
				$\theta = 1.5^\circ$				
Type I	1	−2	2	−1	2	−2	2	−1
Type II	0	1	1	0	0	1	1	0
				$\theta = 1.05^\circ$				
Type I	0	−2	2	0	0	−2	2	0
Type II	−1	1	1	−1	−1	1	1	−1
				$\theta = 0.7^\circ$				
Type I	−2	0	0	2	−2	0	0	...
Type II	0	0	0	0	0	0	0	0

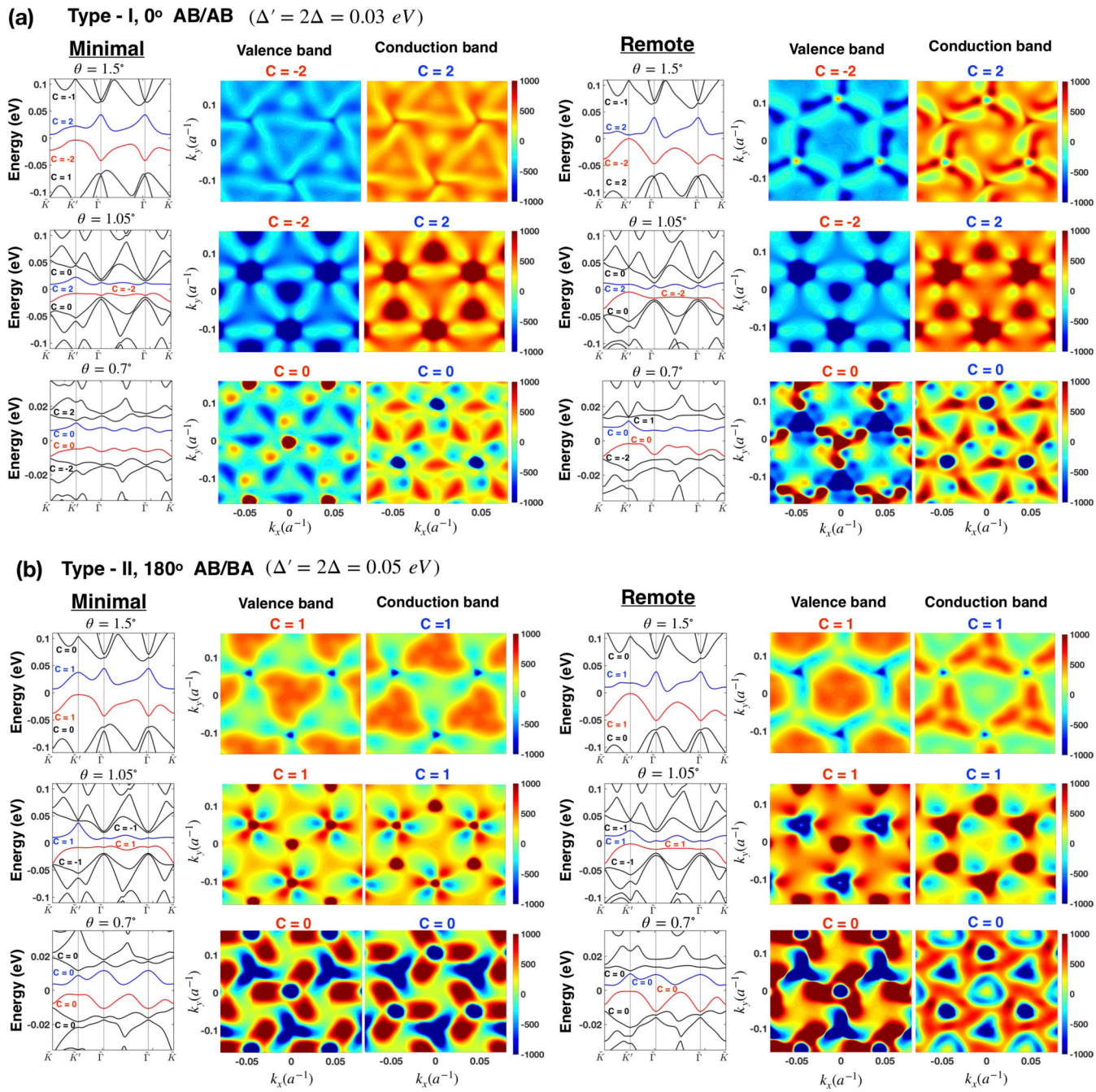

FIG. 10. Band structure and Berry curvature plots for select twist angles $\theta = 0.7°, 1.05°, 1.5°$ and interlayer potential differences within the minimal and remote hopping parameters Hamiltonian model for tBBG, leading to quantitative differences in the bandwidths and associated $\delta_{p/s}$ for the primary and secondary gaps. The results are shown for (a) type I near 0° AB/AB alignment for $\Delta' = 2\Delta = 0.03$ eV and for (b) type II near 180° AB/BA alignment that requires a larger $\Delta' = 2\Delta = 0.05$ eV to simultaneously achieve positive primary and secondary gaps $\delta_{p/s} > 0$. For $\theta \gtrsim 1°$ these two alignments are shown to give distinct $C_\upsilon = \pm 2$ of opposite and $C_\upsilon = 1$ same sign K valley Chern numbers for valence and conduction bands. These qualitative differences in the Chern numbers for the two stacking alignments can be traced to the different associated chiralities of the bands in the top and bottom layers.

valence bands. With proper electric fields we expect that practically all angles spanning the range between 0.4° and 1.6° could host ordered phases. Application of pressure can also enhance the isolation of the bands when used in combination with appropriate electric fields. We have related the interlayer tunneling with external pressure through stacking-dependent interlayer coupling parameters ω and ω' compatible with the EXX+RPA interlayer potentials to capture the interdependence of corrugation and interlayer tunneling in a self-contained manner. A more detailed study that combines the effects of in-plane moiré strains will be addressed elsewhere. Comparisons between the electronic structure between the type I near 0° aligned systems and the type II 180° aligned bi-bilayers indicate that 0° aligned systems generally require

weaker electric fields to achieve optimal flat band systems prone to interaction-driven ordered phases, and give rise to distinct valley Chern number phase diagrams.

Note added. Related experiments and theory are Refs. [63–65] and Refs. [66–69].

ACKNOWLEDGMENTS

We acknowledge helpful discussions with S. Kahn, F. Wu, and M. Koshino. This work was supoprted by Samsung Science and Technology Foundation under Project No. SSTF-BA1802-06 for J.J. Financial support is acknowledged for N.R.C. from the Korean National Science Foundation through Grant No. NRF-2016R1A2B4010105, for B.L.C. by the Basic Science Research Program through the National Research Foundation of Korea (NRF) funded by the Ministry of Education Grants No. 2018R1A6A1A06024977 and No. NRF-2017R1D1A1B03035932. This research was supported in part by the U.S. National Science Foundation under Grant No. NSF PHY-1748958.

[1] Y. Cao, V. Fatemi, A. Demir, S. Fang, S. L. Tomarken, J. Y. Luo, J. D. Sanchez-Yamagishi, K. Watanabe, T. Taniguchi, E. Kaxiras, R. C. Ashoori, and P. Jarillo-Herrero, Nature (London) **556**, 80 (2018).

[2] K. Kim, A. DaSilva, S. Huang, B. Fallahazad, S. Larentis, T. Taniguchi, K. Watanabe, B. J. LeRoy, A. H. MacDonald, and E. Tutuc, Proc. Natl. Acad. Sci. USA **114**, 3364 (2017).

[3] Y. Cao, V. Fatemi, S. Fang, K. Watanabe, T. Taniguchi, E. Kaxiras, and P. Jarillo-Herrero, Nature (London) **556**, 43 (2018).

[4] M. Yankowitz, S. Chen, H. Polshyn, K. Watanabe, T. Taniguchi, D. Graf, A. F. Young, and C. R. Dean, Science **363**, 1059 (2019).

[5] Y. Cao, D. Chowdhury, D. Rodan-Legrain, O. Rubies-Bigora, K. Watanabe, T. Taniguchi, T. Senthil, and P. Jarillo-Herrero, arXiv:1901.03710.

[6] P. Zubko, S. Gariglio, M. Gabay, P. Ghosez, and J.-M. Triscone, Annu. Rev. Condens. Matter Phys. **2**, 141 (2011).

[7] R. Bistritzer and A. H. MacDonald, Proc. Natl. Acad. Sci. USA **108**, 12233 (2011).

[8] M. Ochi, M. Koshino, and K. Kuroki, Phys. Rev. B **98**, 081102(R) (2018).

[9] J. M. Pizarro, M. J. Calderón, and E. Bascones, arXiv:1805.07303.

[10] J. W. F. Venderbos and R. M. Fernandes, Phys. Rev. B **98**, 245103 (2018).

[11] B. Padhi, C. Setty, and P. Phillips, Nano Lett. **18**, 6175 (2018).

[12] M. Koshino, N. F. Q. Yuan, T. Koretsune, M. Ochi, K. Kuroki, and L. Fu, Phys. Rev. X **8**, 031087 (2018).

[13] J. Kang and O. Vafek, Phys. Rev. X **8**, 031088 (2018).

[14] J. Kang and O. Vafek, arXiv:1810.08642.

[15] M. Fidrysiak, M. Zegrodnik, and J. Spalek, Phys. Rev. B **98**, 085436 (2018).

[16] B. Roy and V. Juricic, Phys. Rev. B **99**, 121407(R) (2019).

[17] T. Huang, L. Zhang, and T. Ma, Sci. Bull. **64**, 310 (2019).

[18] S. Ray, J. Jung, and T. Das, Phys. Rev. B **99**, 134515 (2019).

[19] C.-C. Liu, L.-D. Zhang, W.-Q. Chen, and F. Yang, Phys. Rev. Lett. **121**, 217001 (2018).

[20] T. J. Peltonen, R. Ojajärvi, and T. T. Heikkilä, Phys. Rev. B **98**, 220504(R) (2018).

[21] D. M. Kennes, J. Lischner, and C. Karrasch, Phys. Rev. B **98**, 241407(R) (2018).

[22] H. Isobe, N. F. Q. Yuan, and L. Fu, Phys. Rev. X **8**, 041041 (2018).

[23] Y.-Z. You and A. Vishwanath, arXiv:1805.06867.

[24] H. C. Po, L. Zou, A. Vishwanath, and T. Senthil, Phys. Rev. X **8**, 031089 (2018).

[25] F. Wu, A. H. MacDonald, and I. Martin, Phys. Rev. Lett. **121**, 257001 (2018).

[26] F. Guinea and N. R. Walet, Proc. Natl. Acad. Sci. USA **115**, 13174 (2018).

[27] J. Gonzalez and T. Stauber, Phys. Rev. Lett. **122**, 026801 (2019).

[28] Y. Su and S.-Z. Lin, Phys. Rev. B **98**, 195101 (2018).

[29] B. Lian, Z. Wang, and B. A. Bernevig, arXiv:1807.04382.

[30] E. Laksono, J. N. Leaw, A. Reaves, M. Singh, X. Wang, S. Adam, and X. Gu, Solid State Commun. **282**, 38 (2018).

[31] Q. K. Tang, L. Yang, D. Wang, F. C. Zhang, and Q. H. Wang, Phys. Rev. B **99**, 094521 (2019).

[32] A. Kerelsky, L. McGilly, D. M. Kennes, L. Xian, M. Yankowitz, S. Chen, K. Watanabe, T. Taniguchi, J. Hone, C. Dean, A. Rubio, and A. N. Pasupathy arXiv:1812.08776.

[33] G. Chen, L. Jiang, S. Wu, B. Lyv, H. Li, K. Watanabe, T. Taniguchi, Z. Shi, J. Jung, Y. Zhang, and F. Wang, Nat. Phys. **15**, 237 (2019).

[34] G. Chen, A. L. Sharpe, P. Gallagher, I. T. Rosen, E. Fox, L. Jiang, B. Lyu, H. Li, K. Watanabe, T. Taniguchi, J. Jung, Z. Shi, D. Goldhaber-Gordon, Y. Zhang, and F. Wang, arXiv:1901.04621.

[35] G. Chen, A. L. Sharpe, E. J. Fox, Y.-H. Zhang, S. Wang, L. Jiang, B. Lyu, H. Li, K. Watanabe, T. Taniguchi, Z. Shi, T. Senthil, D. Goldhaber-Gordon, Y. Zhang, and F. Wang, arXiv:1905.06535.

[36] B. L. Chittari, G. Chen, Y. Zhang, F. Wang, and J. Jung, Phys. Rev. Lett. **122**, 016401 (2019).

[37] F. Zhang, J. Jung, G. A. Fiete, Q. Niu, and A. H. MacDonald, Phys. Rev. Lett. **106**, 156801 (2011).

[38] L. Xian, D. M. Kennes, N. Tancogne-Dejean, M. Altarelli, and A. Rubio, arXiv:1812.08097.

[39] S. Javvaji *et al.* (unpublished).

[40] M. H. Naik and M. Jain, Phys. Rev. Lett. **121**, 266401 (2018).

[41] In this work, we loosely use the term flat bands to refer to the sufficiently narrow bandwidth low-energy bands where an effective Coulomb interaction U versus bandwidth W ratio satisfies $U/W \gtrsim 1$.

[42] Y.-H. Zhang, D. Mao, Y. Cao, P. Jarillo-Herrero, and T. Senthil, Phys. Rev. B **99**, 075127 (2019).

[43] J. M. B. Lopes dos Santos, N. M. R. Peres, and A. H. Castro Neto, Phys. Rev Lett. **99**, 256802 (2007).

[44] S. Shallcross, S. Sharma, E. Kandelaki, and O. A. Pankratov, Phys. Rev. B **81**, 165105 (2010).

[45] P. Moon and M. Koshino, Phys. Rev. B **87**, 205404 (2013).
[46] S. Fang and E. Kaxiras, Phys. Rev. B **93**, 235153 (2016).
[47] J. Jung, A. Raoux, Z. Qiao, and A. H. MacDonald, Phys. Rev. B **89**, 205414 (2014).
[48] J. Jung and A. H. MacDonald, Phys. Rev. B **89**, 035405 (2014).
[49] J. Jung and A. H. MacDonald, Phys. Rev. B **87**, 195450 (2013).
[50] D. Wong, Y. Wang, J. Jung, S. Pezzini, A. M. DaSilva, H.-Z. Tsai, H. S. Jung, R. Khajeh, Y. Kim, J. Lee, S. Kahn, S. Tollabimazraehno, H. Rasool, K. Watanabe, T. Taniguchi, A. Zettl, S. Adam, A. H. MacDonald, and M. F. Crommie, Phys. Rev. B **92**, 155409 (2015).
[51] E. McCann and V. I. Falko, Phys. Rev. Lett. **96**, 086805 (2006)
[52] N. Leconte, J. Jung, S. Lebègue, and T. Gould, Phys. Rev. B **96**, 195431 (2017).
[53] J. Jung, A. M. DaSilva, A. H. MacDonald, and S. Adam, Nat. Commun. **6**, 6308 (2015).
[54] B. L. Chittari, N. Leconte, S. Javvaji, and J. Jung, Elect. Struct. **1**, 015001 (2019).
[55] A. M. DaSilva, J. Jung, S. Adam, and A. H. MacDonald, Phys. Rev. B **91**, 245422 (2015).
[56] M. Yankowitz, J. Jung, E. Laksono, N. Leconte, B. L. Chittari, K. Watanabe, T. Taniguchi, S. Adam, D. Graf, and C. R. Dean, Nature (London) **557**, 404 (2018).
[57] S. Carr, S. Fang, P. Jarillo-Herrero, and E. Kaxiras, Phys. Rev. B **98**, 085144 (2018).
[58] See Supplemental Material at http://link.aps.org/supplemental/10.1103/PhysRevB.99.235417 for complementary information on (1) the pressure-dependent bandwidth and gaps phase diagram, (2) the parametrization of the interlayer distance-dependent pressure and tunneling for the P versus ω relationship, and (3) the low-energy bands formulation of the Hamiltonian.
[59] Y.-H. Zhang, D. Mao, and T. Senthil, arXiv:1901.08209.
[60] N. Bultinck, S. Chatterjee, and M. P. Zaletel, arXiv:1901.08110.
[61] F. Wu, T. Lovorn, E. Tutuc, and A. H. MacDonald, Phys. Rev. Lett. **121**, 026402 (2018).
[62] D. Xiao, M. C. Chang, and Q. Niu, Rev. Mod. Phys. **82**, 1959 (2010).
[63] X. Liu, Z. Hao, E. Khalaf, J. Y. Lee, K. Watanabe, T. Taniguchi, A. Vishwanath, and P. Kim, arXiv:1903.08130.
[64] C. Shen, N. Li, S. Wang, Y. Zhao, J. Tang, J. Liu, J. Tian, Y. Chu, K. Watanabe, T. Taniguchi, R. Yang, Z. Y. Meng, D. Shi, and G. Zhang, arXiv:1903.06952.
[65] Y. Cao, D. Rodan-Legrain, O. Rubies-Bigorda, J. M. Park, K. Watanabe, T. Taniguchi, and P. Jarillo-Herrero, arXiv:1903.08596.
[66] Y. W. Choi and H. J. Choi, arXiv:1903.00852.
[67] J. Y. Lee, E. Khalaf, S. Liu, X. Liu, Z. Hao, P. Kim, and A. Vishwanath, arXiv:1903.08685.
[68] M. Koshino, Phys. Rev. B **99**, 235406 (2019)..
[69] J. Liu, Z. Ma, J. Gao, and X. Dai, arXiv:1903.10419.